Materials Science & Engineering A 840 (2022) 142898

Contents lists available at ScienceDirect

Materials Science & Engineering A

journal homepage: www.elsevier.com/locate/msea

Fatigue crack propagation behavior of a micro-bainitic TRIP steel

I. Burda [a,*], K. Zweiacker [a], A. Arabi-Hashemi [a], P. Barriobero-Vila [b], A. Stutz [a], R. Koller [a], H. Roelofs [c], L. Oberli [c], M. Lembke [c], C. Affolter [a], C. Leinenbach [a]

[a] *Empa, Swiss Federal Laboratories for Materials Science and Technology, Dübendorf, Switzerland*
[b] *German Aerospace Center (DLR), Cologne, Germany*
[c] *Steeltec AG, Emmenbrücke, Switzerland*

ARTICLE INFO

Keywords:
TRIP steel
Grain refinement
Fatigue crack propagation
High-energy synchrotron X-ray diffraction

ABSTRACT

Controlling the grain size of steels is an effective way for tailoring their mechanical properties, such as yield strength, impact toughness, and ductility. In this study, a new industrial thermomechanical treatment was applied to a low-alloyed TRIP-assisted bainitic steel 13MnSiCr7 to achieve a substantial microstructural refinement. In this way the average grain size of the new micro-bainitic steel was decreased from ~25 µm to ~5 µm. Fatigue tests were carried out in order to investigate the influence of this new thermomechanical treatment on crack propagation behavior. Besides electron backscatter diffraction (EBSD), vibrating sample magnetometry (VSM), and high-energy synchrotron X-ray diffraction (HEXRD) were used to study the microstructure in the vicinity of the fatigue crack tip. The applicability of each method for detecting the martensitic transformation is discussed. In addition, the contribution of the martensitic transformation to fracture toughness was assessed on the basis of the results obtained by HEXRD.

1. Introduction

In the last two decades, a broad variety of advanced high strength steels (AHSS) has been developed, including the so-called TRansformation Induced Plasticity (TRIP) steels. Depending on their chemical composition and thermomechanical processing, the microstructure of these steels may consist of ferrite, bainite, martensite and residual austenite [1]. The key benefit of this type of steels is a combination of high strength and ductility, allowing the manufacturing of light-weight components with considerable energy absorption properties during impact.

Whereas classical TRIP steels found applications in flat products with modest strength and good formability, new TRIP-assisted bainitic steels with higher strength have gained an increasing interest for long products and automotive applications over the last decade. It was found that components manufactured out of TRIP-assisted bainitic steels often exhibit longer lifetimes under realistic cyclic load collectives comparing with conventional quenched and tempered (Q&T) steels [2]. When applying single overloads, the steel exhibits local hardening due to phase transformation from residual austenite to martensite. Consequently, the lifetime of the component is increased “in-situ” [3,4]. This new class of steel can be produced from hot working temperatures applying natural cooling. Additional heat treatments like Q&T can be omitted, which eventually leads to reduction of costs and increased sustainability. However, the low cooling rate conditions in large components might cause coarse granular microstructure, which may lead to larger scatter of fatigue properties. This potential drawback can be avoided by reducing the hot deformation temperature during thermomechanical treatment in order to refine the prior austenite grains.

Recently, new industrial technologies in the production of hot rolled bars have allowed refinement of prior austenite grains in the order of few microns. In comparison with ferritic-pearlitic steels, the production of grain refined continuously cooled bainitic steels is not a trivial task. The small prior austenite grain size in combination with the available cooling schedule define the range of possible steel compositions. Typical commercially available continuously cooled bainitic steels do not fulfill these requirements. In the present work a steel alloy composition, namely 13MnSiCr7, was tailored allowing the production of the first micro-bainitic TRIP steel.

In real automotive steel parts under dynamic loads local plastic deformation might occur due to external overloads or stress concentrations (e.g. edges, notches, etc). Further cyclic loading, and the associated damage accumulation, may lead to fatigue crack initiation. At the same time, strain fields induced by the plastic deformation in the

---

[*] Corresponding author.
E-mail address: iurii.burda@empa.ch (I. Burda).

https://doi.org/10.1016/j.msea.2022.142898
Received 2 November 2021; Received in revised form 23 February 2022; Accepted 24 February 2022

vicinity of crack tip may trigger the TRIP effect. Residual austenite partially transforms into martensite, and the resulting volume expansion introduces compressive stresses. The latter should restrict further crack growth, and, as a consequence, the service life of the considered part increases. It is reasonable to believe that the spatial as well as size distribution of the residual austenite phase determines the magnitude of this effect [5].

From previous studies it is supposed that the refinement of the prior austenite grains also has a positive effect on the fatigue properties. Mughrabi and Höppel showed that Wöhler curves for materials with conventional and finer grain sizes differ [6]. In the range of high cycle fatigue (HCF) and low total strain, the fatigue behaviour is mainly determined by the strength of the material. Wöhler curves in this regime can be very well described with the Basquin approach. In the range of finite life (low cycle fatigue, LCF), the fatigue behaviour depends on ductility and on the ability of the material to withstand high cyclic strains.

Niendorf et al. [7–9] investigated the cyclic stability of a ferritic interstitial-free (IF) steel in the LCF range. Due to the high density of high-angle grain boundaries and the presence of fine grain boundary precipitates, cyclic softening was no longer observed after sufficient forming during strain-controlled cyclic testing. Additionally, a significant increase of the endurance limit was observed. One of the first investigations on the fatigue behaviour of fine-grained ferritic-pearlitic steels was done by Sawai et al. [10]. Here, the endurance limit of the considered steel with a carbon content of 0.15 wt% could be increased by more than 50%. Chapetti et al. [11] confirmed this finding, but observed that small grains can lead to a higher notch sensitivity. On the other hand, the process of severe plastic deformation, which is used for the production of fine grained steels, might introduce local shear bands or cracks [12–16]. Therefore, phase transformations driven by thermal processes are often employed for the production of fine-grained steels. Investigations of cyclic properties of steels produced by severe plastic deformation are rare [17–19].

These mentioned research works considered ferritic-pearlitic microstructures and austenite grain sizes of 1 μm or below. However, prior austenite grain sizes of such dimensions are not compatible with the bainite transformation under industrial natural cooling conditions. In this case a prior austenite grain size in the order of 5 μm is considered to be more realistic and adequate.

In the present work, the fatigue crack propagation behaviour of TRIP-assisted bainitic steel 13MnSiCr7 in two processing conditions with different microstructures, particularly grain size, was studied. The reference steel 13MnSiCr7 [20] was conventionally hot rolled at 1100 °C. The new micro-bainitic steel was produced utilizing a thermomechanical hot rolling treatment designated as XTP® [21,22]. The corresponding microstructural changes were studied by scanning electron microscopy (SEM), electron backscatter diffraction (EBSD), vibrating sample magnetometry (VSM) and high energy synchrotron X-ray diffraction (HEXRD). Finally, an assessment of the contribution of TRIP effect to the fracture toughness for both steels is discussed.

2. Materials and methods

2.1. Material

Steel grade 13MnSiCr7 was industrially produced at Steeltec (80 ton heat, continuously casting 150 × 150 mm^2 billets and hot rolling bars). The nominal steel composition is given in Table 1. A low carbon content was chosen to achieve a high bainite content. Microalloying elements (Nb, V) were added to reach an acceptable high static strength level.

The conventionally hot rolled reference bar (called "STD") was 31 mm in diameter. During the rolling process a mean prior austenite grain size of ~25 μm was achieved.

The refinement of microstructure of the STD material was achieved by subjecting the bars of reference steel (Ø40 mm) to additional thermomechanical treatment. A new hot rolling technology, called XTP®, uses severe deformation in one single rolling step within a temperature window from 700 to 850 °C to refine the austenite grains [20,21,23,24]. A full disclosure of the processing parameters is not provided due to proprietary reasons. The schematic layout of the rolling line is shown in Fig. 1. The first phase implies an induction heating of an input bar to the austenitization temperature of ~950 °C. This is followed by isothermal holding for the temperature homogenization within the bar. The forming stage is carried out by means of a rolling mill, which consists of three cone-shaped rolls. The mill induces severe plastic deformation within the bar, leading to significant grain refinement of its microstructure. In this study, the cross-section of the bar was reduced by one single deformation step from initial Ø40 mm to Ø30 mm. After the forming stage the temperature ~800 °C of the bar was measured. Under these conditions, a mean prior austenite grain size of ~5 μm is expected. The micro-bainitic TRIP-assisted steel bar after thermomechanical treatment is hereafter referred to as "TM". After the hot rolling a fast cooling using three water boxes (200–300 l/min water consumption) was applied. As a consequence a harder, martensite-rich surface layer is obtained. Micro-hardness measurements show that the hardness falls within the first 5 mm from the surface to a constant hardness value which is comparable to the conventionally hot rolled steel (STD). The presented and discussed results in this study were obtained within this core zone with constant hardness. The microstructure as seen at a mid-radius position and as shown in Fig. 1 is, therefore, representative for the performed investigations. Additionally, the investigations of STD bars Ø31 mm and Ø40 mm revealed their almost identical microstructures.

The corresponding microstructures at a mid-radius bar position as observed by light optical microscopy are shown in Fig. 1. In order to inhibit the growth of austenite grains after severe deformation at elevated temperatures, the material should be subjected to rapid cooling thereafter. Thus, the changes in processing parameters between STD and TM steels do not only affect the prior austenite grain sizes but also the phase constituents. Although bainite is the dominant phase under both conditions, the conventionally hot rolled material exhibits more ferrite (due to slower cooling rates).

The corresponding properties from static tensile testing are listed in Table 2. The tensile tests were carried out according to Ref. [25] on samples type B10 × 50 [26] with circular cross-section.

2.2. Experimental methods

2.2.1. Fatigue crack propagation

Load-controlled cyclic tests according to Ref. [27] were performed for both materials using compact tension (CT) samples in order to investigate the fatigue crack behavior. As a result, the fatigue crack growth rate was determined as a function of stress intensity factor ΔK for a given R-ratio R = 0.1. The size of the cyclic plastic zone in the vicinity of the crack tip can be controlled by altering the stress intensity factor, which in turn is a function of the crack length and load. This provides an opportunity to analyze the microstructural changes (e.g. phase transformation, residual stresses and strains) near the crack tip, as well as to investigate the influence of those microstructural changes on crack propagation behavior and fatigue properties of material.

Table 1
Chemical composition of steel 13MnSiCr7.

Element	C	Si	Mn	S	Ni	Cr	Mo	V	Nb	Al	N
wt.%	0.14	0.53	1.75	0.01	0.07	0.64	0.01	0.09	0.06	0.03	0.011

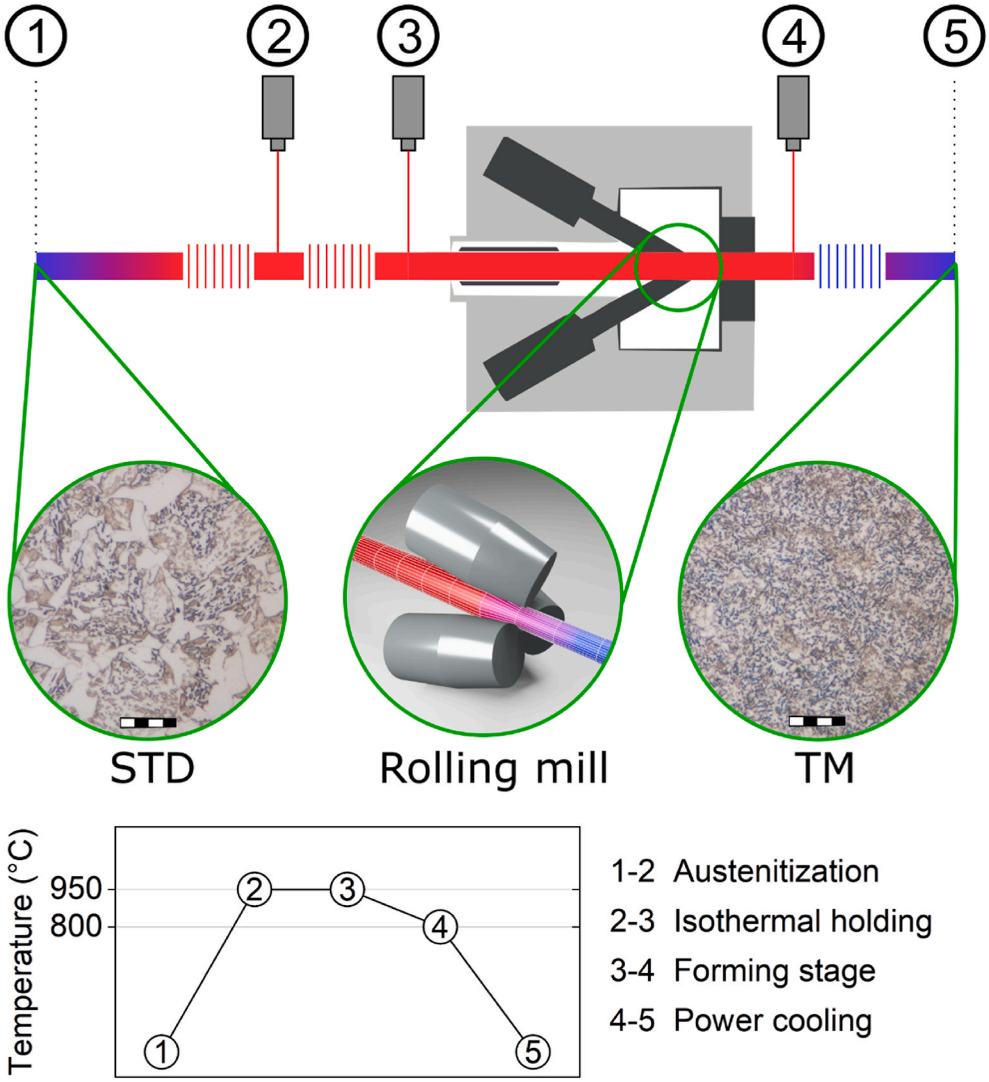

Fig. 1. Schematic of the XTP® rolling line, depicting the micrographs of two investigated steels and a temperature profile during thermomechanical processing. The scale bars on the micrographs are 10 μm.

Table 2
Static mechanical properties of STD and TM steels.

Steel	Yield strength, MPa	Ultimate tensile strength, MPa	Uniform elongation, %	Reduction of cross section, %	Elongation at fracture, %
STD	533	838	9.0	58.0	19.2
TM	526	919	12.0	59.0	21.3

In comparison with the standard CT samples, the geometry of the samples used in this work had to be slightly modified. Due to fairly small diameters of the investigated steel bars (Ø31 mm and Ø30 mm for STD and TM, respectively), the dimensions of the specimens were proportionally scaled down, in order to ensure an adequate sampling (Fig. 2). The CT samples were manufactured using electrical discharge machining in order to prevent the introduction of residual stresses from mechanical machining. The orientation of the notch and the consecutive crack is perpendicular to the axis of the steel bars. Finally, as recommended in Ref. [27], the samples were polished from both sides.

A high-frequency resonance test facility Rumul Mikrotron 654 with a maximal load capacity of ±5 kN was used to investigate the fatigue crack propagation behavior. The testing frequency of resonance testing machines depends on the stiffness of the sample, as it is a part of an oscillating mass-spring system. An increase of crack length causes a decrease of the frequency, as the sample becomes more compliant. The testing frequency was in the range of 120–135 Hz. The crack length was measured from both sides of the sample using traveling microscopes and the average value was calculated.

In order to determine the fatigue crack growth rate as a function of ΔK a combination of two procedures was used: ΔK-decreasing with subsequent ΔK-increasing. At the beginning of the test, ΔK was gradually decreased in order to estimate a part of the Paris region and the threshold ΔK_{th}. The latter one was established, as the crack growth rate $da/dN \leq 10^{-8}$ m/cycle was reached. After that, ΔK was progressively increased for the determination of the Paris region for higher crack propagation rates. Finally, the fracture toughness K_{IC} was determined by quasistatically loading the CT samples with previously grown fatigue crack until failure.

Additionally, a number of crack growth tests were performed to initiate the fatigue crack for various investigations, including VSM, HEXRD, etc. They are summarized in Table 3.

2.2.2. *Topographic characterization*

Topographic investigations of the CT sample surfaces along the fatigue crack were carried out using an optical profilometer Leica DCM8.

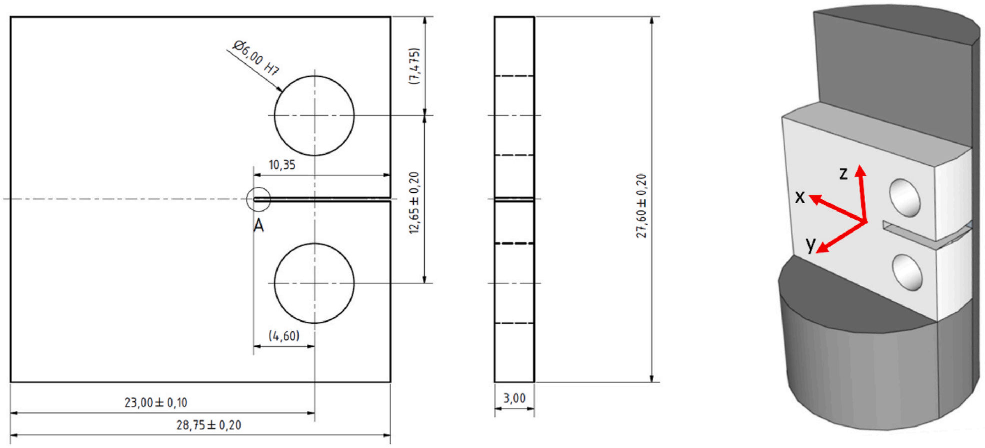

Fig. 2. Sketch of the CT sample and its cutout orientation with respect to the steel bar. The dimensions are given in mm.

Table 3
Summary of CT samples and subsequent investigations.

Sample	Material	Type of crack growth test	Fatigue crack length a, [mm]	Maximum stress intensity ΔK at the crack tip/Range of stress intensity factor ΔK, [MPa m$^{0.5}$]	Subsequent investigations
CT-STD-1	STD	ΔK-decrease with subsequent ΔK increase/ Fracture toughness	11.62	5.6–71.5	Fractography
CT-TM-1	TM	ΔK-decrease with subsequent ΔK increase/ Fracture toughness	11.8	7.2–69.1	Fractography
CT-STD-2	STD	ΔF-constant	13.6	34.8	Topography/ VSM
CT-TM-2	TM	ΔF-constant	13.56	34.6	Topography/ VSM
CT-STD-3	STD	ΔF-constant	12.6	35	HEXRD
CT-TM-3	TM	ΔF-constant	16	45	HEXRD

An array of images of the sample surface was taken while operating the optical profilometer in confocal mode in order to acquire a sufficiently large area. The subsequent reconstruction and stitching of surface topography images was done automatically using the software Leica SCAN 5.4. Post processing and further analysis of acquired topographical data was done using Leica Map 7.4.

2.2.3. Microstructure characterization

EBSD measurements were done on a Hitachi S4800 electron microscope using an electron energy of 20 keV and a 70° sample tilting. The step size for STD steel was chosen to be 250 nm. Due to smaller grain size, the step size of EBSD measurements for TM steel was reduced to 100 nm.

A thorough sample preparation process was chosen to avoid artifacts on the sample surface. Samples were prepared by standard metallography techniques including grinding to P4000 followed by 3 μm and 1 μm diamond suspension polishing and final polishing using 50 nm silica colloidal suspension. During grinding and polishing steps rather lower pressure was favored to avoid triggering the martensitic transformation. This was compensated with extended process time. After each polishing step, the surface of the sample was investigated under the optical microscope to ensure the absence of scratches from the previous steps.

Phase indexing was performed by including both face centered cubic (fcc) and body centered cubic (bcc) crystal structures. Phase maps and kernel average misorientation (KAM) maps were plotted. KAM maps reveal local lattice misorientation associated with strain gradients which can stem from defects or other phases [28]. The SEM images of the fracture surfaces were taken with a FEI NanoSEM230.

2.2.4. Vibrating sample magnetometry

Vibrating sample magnetometry (VSM) measurements [29] were done on a physical property measurement system (PPMS) from Quantum Design. VSM measurements allow to obtain phase fractions of paramagnetic austenitic fcc phase (hereon the term RA and fcc are used interchangeably) and ferromagnetic bcc phase, assuming that cementite is absent in the investigated materials. This assumption has been validated by additional XRD measurements, which showed for all samples only the presence of these two crystal structures. The VSM measurements were done under two conditions. First, the phase fractions were determined in the undeformed state. Afterwards, the VSM measurements were done in the vicinity of a crack tip to determine the deformation induced phase transformation from austenite to martensite.

For all measurements cylindrical samples with weights in the range of 50–100 mg were cut out by using electrical discharge machining. Four different samples were taken from the material in undeformed state at four different positions as shown in Fig. S1 of the supplementary file.

The saturation magnetization was measured by magnetizing samples to 40000 Oe which corresponds to 4 T. The saturation magnetization was obtained from the magnetization curves by fitting the measured data using equation:

$$M = M_s\left(1 - \frac{a}{H} - \frac{b}{H^2}\right) \tag{1}$$

where M is the magnetization, M_s is the saturation magnetization, H is the applied magnetic field, a and b are fitting parameters [30]. The saturation magnetization of α-Fe is $M_s^{Fe} = 218$ emu/g. However, due to the presence of alloying elements, the steel 13MnSiCr7 contains only 95 wt% Fe. As a consequence, it is assumed that the saturation magnetization of the material consisting solely of ferromagnetic bcc phase is $M_s^{bcc} = 0.95 \cdot M_s^{Fe} = 207$ emu/g. The fraction of residual austenite is then calculated according to

$$V_{RA} = 1 - \frac{M_s}{M_s^{bcc}} \tag{2}$$

2.2.5. High energy synchrotron X-ray diffraction

High energy synchrotron X-ray diffraction (HEXRD) was performed at the P07-HEMS beamline of PETRAIII, Deutsches-Elektronen-Synchrotron (DESY) [31], by using the experimental parameters summarized in Table 4. A previously tested CT sample was fixed in a stepping xyz stage as shown in Fig. 3a. The region in the vicinity of the crack tip was scanned perpendicularly to the X-ray beam using a step size of 0.2 mm in z and 0.5 mm in x direction (Fig. 3b). The entire Debye-Scherrer rings (Fig. 3c) were acquired in transmission mode from each point of the area indicated in Fig. 3b. The acquired diffraction images were segmented into 10 deg slices perpendicular and parallel to the crack growth direction (red slices in Fig. 3c). After azimuthal integration of the segments, the resulting diffraction information was quantitatively evaluated for phase fraction and change in lattice parameter by Rietveld refinement as implemented in the TOPAS software package.

3. Results

3.1. Electron back scattering diffraction (EBSD)

The EBSD mapping was performed to determine the amount of residual austenite. Samples for EBSD measurements were taken from the center of bars for both STD and TM materials. All data points with a confidence index smaller than 0.1 were removed. The EBSD phase maps of both STD and TM steels in Fig. 4a and Fig. 4c show nearly fully bcc crystal structures with very insignificant amount of confidently indexed fcc regions. In bainitic TRIP-assisted steels the residual austenite can appear in block and lamellar forms, both of which exhibit high degree of lattice distortion caused by interstitial C atoms. It is possible, that at least part of the unindexed data points on the phase maps may be regarded as blocks of residual austenite. This indicates the limitation of the EBSD method, as both STD and TM steels are expected (and will be proven later) to contain bigger fraction of residual austenite.

The KAM maps were plotted to further examine the materials' microstructure (see Fig. 4b and d). Grains that encompass insignificant misorientation of less than 1° (homogeneously blue regions) are ferrite. The volume differences between bainite and residual austenite cause localization of orientation gradients near phase boundaries [32]. Thus, the regions mapped in green are most probably the combination of bainitic ferrite and lamellar residual austenite. Due to the morphology and small size, the grains of the latter were not clearly identified as fcc crystals.

3.2. Fatigue crack propagation behavior

The results of the fatigue crack growth rate as a function of stress intensity factor ΔK of two CT samples, namely CT-STD-1 and CT-TM-1, are presented in Fig. 5. The Paris region represents a stable crack growth condition. The experimental results indicate a slower crack propagation in TM steel compared to STD. Furthermore, the threshold value of the stress intensity factor ΔK_{th} is higher for TM steel. This means that under the same loading conditions the TM steel will tolerate longer cracks without further growth than STD (or otherwise can withstand higher loading, provided the same crack length in both materials).

3.3. Topography of the surface along the fatigue crack

Due to the substantial difference in grain size between STD and TM, it was interesting to compare the size of the cyclic plastic zones near the fatigue crack tip. For this purpose, two CT-samples (CT-STD-2 and CT-TM-2) were produced with similar crack lengths and stress intensity factors using the same constant loading amplitude. Thus, as the crack propagated through the sample, the stress intensity factor at its tip increased. After that, the samples were investigated using an optical profilometer. The comparison of surface topography along the fatigue crack as well as the overview images of the cracks are shown for STD and TM steels in Fig. 6.

As the fatigue crack propagates through the material, it causes extensive plastic deformation creating the cyclic plastic zone at its tip. The size of this region is proportional to the magnitude of the stress intensity factor ΔK. Consequently, the progressively increasing stress intensity factor ΔK in the CT-samples CT-STD-2 and CT-TM-2 caused an expansion of the plastic zone. This is manifested as an enlargement of the valley/groove along the path of fatigue crack (Fig. 6). After extracting the surface profiles perpendicular to the crack path through the point of the fatigue crack tip it is obvious that the plastic deformation in the sample CT-STD-2 is more pronounced than in CT-TM-2, as this valley is both deeper and wider. It is also worth noting that the fatigue crack path in the STD sample is more jagged than in the TM sample.

3.4. Vibrating sample magnetometry

The undeformed STD steel has a homogeneously distributed fcc phase varying between 7.5 and 8.5 vol% (average 8 vol %). For the undeformed TM steel the fcc phase is homogeneously distributed in the inside of the bar with a phase fraction between 10 and 11 vol% (average 10.5 vol%), while at the peripheral layers of the bar the fcc phase content drops to only 1 vol% (see Fig. S3 in the supplementary file).

Cylindrical (bulk) VSM samples were taken in perpendicular direction from the crack tip. Fig. S2 in the supplementary document shows the location of the measured samples in the vicinity of the crack tip. For the TM steel, a total of five specimens at 0 mm, 1 mm and 2 mm on both sides from the crack were used, while for the STD steel only three cylindrical samples were prepared (at 0 mm, 1 mm and 2 mm distance on one side from the crack).

The TM samples show an increase of the fcc content with increasing distance from the crack tip, which is an indicator of the phase transformation. At the crack tip, the amount of residual austenite is around 6 vol% (Fig. 7), which is lower when compared with the sample in the undeformed state. However, this value might be even lower than 6 vol% directly at the crack tip itself, considering the relatively large volume of the VSM samples. The diameter of the VSM samples is ~0.5 mm, which is on the order of magnitude of the plastic zone near the crack tip. A similar trend, although with somewhat lower values, is observed in the STD material, for which a value of 5 vol% residual austenite was measured near the crack tip (Fig. 7). As in the case of the TM sample, this drop is likely due to the fcc to bcc transformation.

Table 4
HEXRD experimental parameters.

Energy [keV]	Wavelength [Å]	Slit-aperture size [mm]	Step size [mm]	Sample-detector distance [mm]	Acquisition time [s]	Detector
100	0.124	0.2 × 0.2	0.2 in z 0.5 in x	1543.59	Sum of 5 images with an exposure time of 0.5s	Perkin Elmer XRD 1621 2048 × 2048px

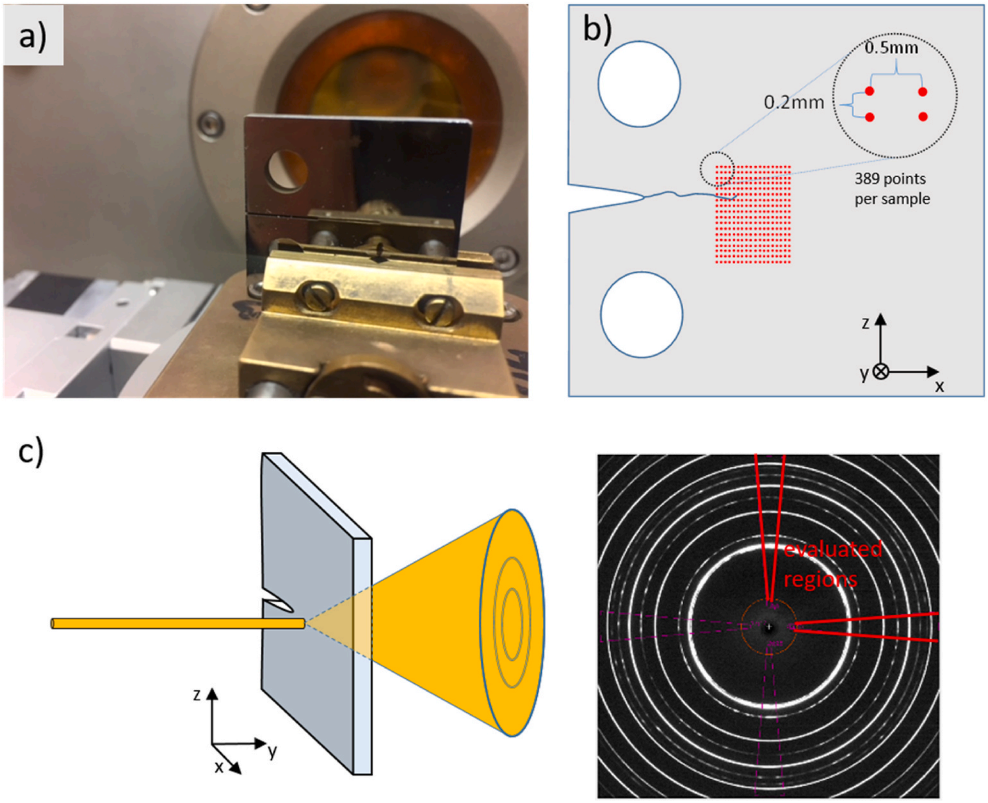

Fig. 3. Employed HEXRD setup at P01-PETRAIII: a) sample setup on XYZ stage b) acquisition matrix covering an area of 5 × 7 mm (X × Z), c) orientation of the sample and segmentation of the Debye-Scherrer rings.

3.5. *High-energy synchrotron X-ray diffraction*

HEXRD experiments were utilized to get insight on quantitative bulk phase fraction and residual strains after interrupted fatigue crack growth experiments of the CT samples CT-STD-3 and CT-TM-3. Fig. 8a shows the color-coded maps of the selected region of the fcc phase fraction distribution obtained by the HEXRD in the TM steel. The very fine-grained structure and the equally small distributed fcc phase lead to accurate phase identification during Rietveld refinement. Due to the small grains and homogenous distribution of the fcc phase, an average residual austenite content in TM material was determined to be ~11 vol% (Fig. 8b), which corresponds well with the VSM measurements. The presented phase fractions were determined by Rietvelt refinement fitting the bcc and fcc phase simultaneously. As shown in Fig. 8c, along the indicated crack path (black line) a clear change in microstructure and an increased amount bcc phase is observed, indicating the occurred phase change. A minimum amount of the residual austenite of ~1.8 vol % is found right in front of the crack tip.

Fig. 9 shows the average lattice strains for the fcc and bcc phases perpendicular (ε_{zz}) and parallel (ε_{xx}) to the crack propagation direction in the TM steel. The lattice strain was calculated using the relative variation of the refined lattice parameter (a) across the sample in the usual way, i.e.

$$\varepsilon = \frac{a - a_0}{a_0} \tag{3}$$

This approach has the advantage that, by including many peaks in the refinement, the measured strains are likely to be representative of the macroscopic response, free from significant elastic or plastic anisotropy effects. The unstrained lattice parameter (a_0) was obtained from the averaged far-field measurement in the unloaded state.

The strain fields in the TM steel indicate pronounced compressive strains at the crack tip in both x- and z-directions, with more pronounced compressive strain field in the fcc phase.

For the STD steel with a much larger grain size as evident from previously shown EBSD images (see Fig. 4), the equivalent phase and strain maps are shown in Fig. 10 and Fig. 11. Islands of fcc rich and poor regions are distributed equidistantly in the observed microstructure, making it challenging to directly identify phase transformation. Due to the larger grains and the coarser distribution of fcc islands in the STD samples, it is more difficult to clearly recognize a crack path in the phase map. However, the residual strain fields in x and z direction are still clearly visible. A clear compressive strain field in front of a more jagged crack path is observed, presenting a maximum intensity right in front of the crack tip. The fcc phase in the bulk material of STD steel seems to be under residual tensile strain perpendicular to the crack propagation direction (i.e. parallel to the axis of the bar) and compressive strain along the crack (i.e. normal to the axis of the bar). One of the possible explanations of these residual stain fields could be a texture of the material of the bar. However, in this case the compensating strain fields would be expected in the bcc phase, which are clearly absent, as the bulk material in Fig. 11a and b is roughly strain free. At the same time, the fatigue crack is clearly visible in Fig. 11d, and manifest itself as tensile strain along the crack path.

The residual elastic stresses σ_{xx} and σ_{zz} were calculated based on the estimated strain fields using the following equation

$$\sigma_{ij} = \frac{E}{1+\nu}\left(\varepsilon_{ij} + \frac{\nu}{1-2\nu}(\varepsilon_{11} + \varepsilon_{22} + \varepsilon_{33})\right) \tag{4}$$

Where σ_{ij} and ε_{ij} are stress and strain along the chosen axes, E is the modulus of elasticity (in this study $E = 200$ GPa and $E = 212$ GPa were used for fcc and bcc phase, respectively), ν is the Poisson's ratio (here, $\nu = 0.28$), and $\varepsilon_{11}, \varepsilon_{22}, \varepsilon_{33}$ are strains in three orthogonal directions.

Considering the plane strain conditions near the crack tip (i.e. $\varepsilon_{yy} = 0$), the stress σ_{yy} was calculated as follows

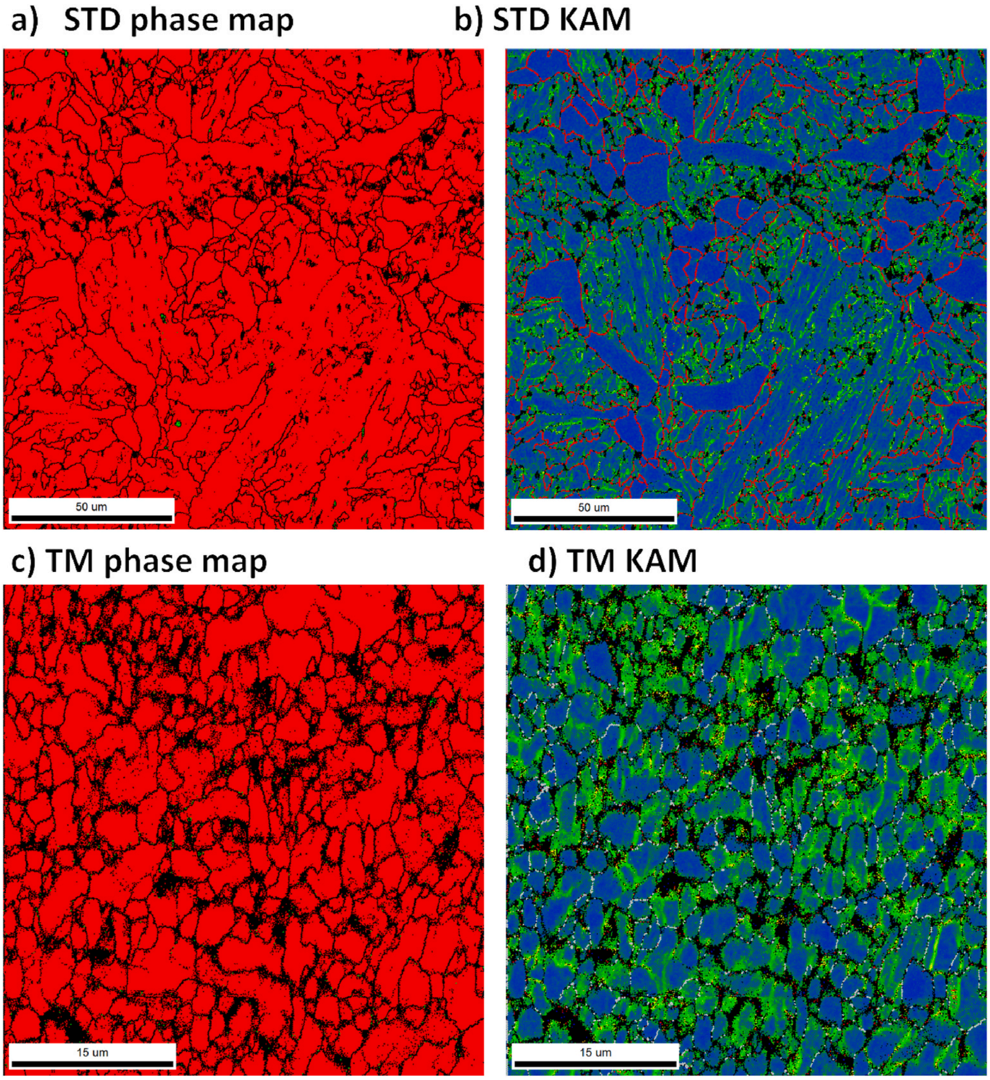

Fig. 4. a) and c) EBSD phase maps of STD and TM steels. Red and green colors indicate bcc and fcc crystal structures respectively. b) and d) kernel average misorientation. Grain boundaries are shown in red. Note the difference in magnification between a), b) and c), d) reflecting the smaller grain size of TM steel. (For interpretation of the references to color in this figure legend, the reader is referred to the Web version of this article.)

$$\sigma_{yy} = \nu(\sigma_{xx} + \sigma_{zz}) \tag{5}$$

The calculated residual stresses near the fatigue crack tip in fcc and bcc phases for both STD and TM materials are given in Table 5.

The estimated residual stresses in TM sample are much higher than in STD, which can be contributed to significantly higher stress intensity factor in the former sample. In the STD steel the fcc phase near the crack tip appears to be under tensile stress, while the bcc phase in the vicinity of the crack tip is under compression. The tensile stress component in fcc phase evidently results from the tensile strain field that was discussed above. On the contrary, in the TM steel both fcc and bcc phases are under considerably higher compressive stresses.

A significant contributing factor to the stability of retained austenite is its carbon content, which can be estimated using empirical relationship [33] to austenite lattice parameter

$$C = \frac{a - 0.3555}{0.004}, \tag{6}$$

where a is austenite lattice parameter in nm.

From the HEXRD measurements on the undeformed area of material (1.5×5 mm^2) the average austenite lattice parameter and its carbon content were calculated for both STD and TM steels (Table 6). The carbon content in residual austenite in STD steel is somewhat higher.

3.6. Fractography

For a better understanding of the fatigue crack propagation behavior, fractographic investigations of the CT sample CT-STD-1 were carried out in the SEM. The fractograms presented here were taken in the zones of the cracks surface, where the stress intensity factor was in the range 32–36 MPa m$^{0.5}$. On a somewhat larger scale, the fracture surface of CT-STD-1 seems to be fairly rough (Fig. 12 a). The detailed investigation revealed quite pronounced striation lines (Fig. 12 b), which indicates stable crack growth. Over a length of 4 μm around 20–24 lines were counted, which would result in a crack propagation rate in the range of 160–200 nm/cycle. This corresponds fairly well to the actually measured crack propagation rates in that region. Furthermore, multiple secondary cracks perpendicular to the main fatigue crack were observed, which indicates crack brunching.

Further investigations of the fracture surface revealed additional features. Multiple regions of brittle cleavage fracture can be observed. These are indicated in Fig. 12a and c with red ellipses, with no visible striation lines on them. It is possible that these cleavage fracture zones are ferrite grains, considering their size (approx. 40–80 μm) and

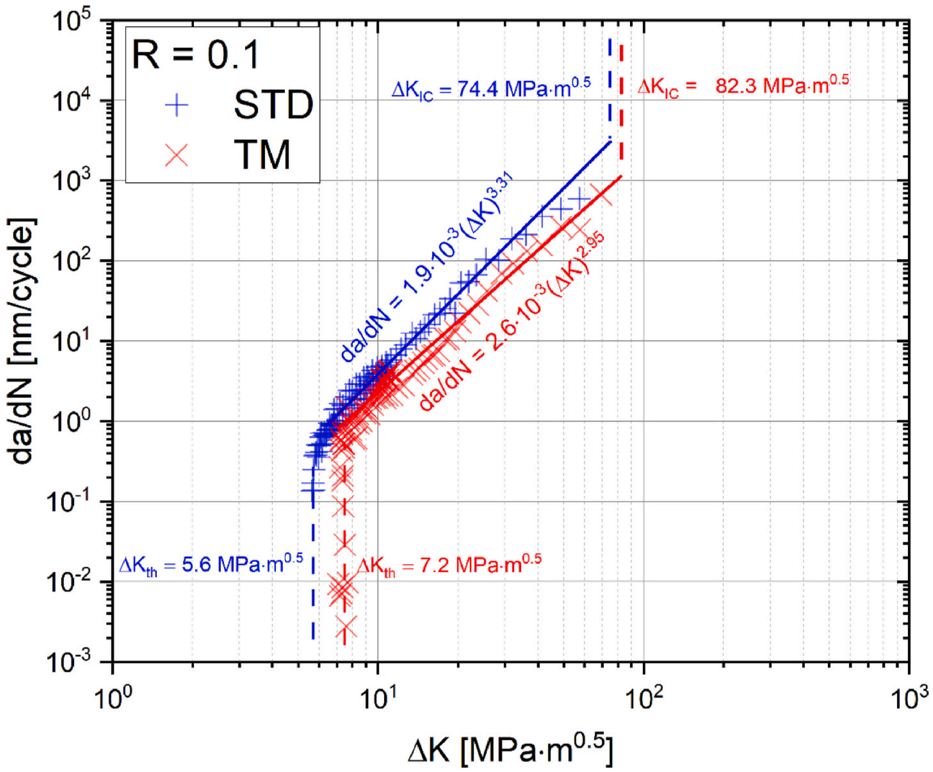

Fig. 5. Fatigue crack growth rate as a function of ΔK for STD and TM steel.

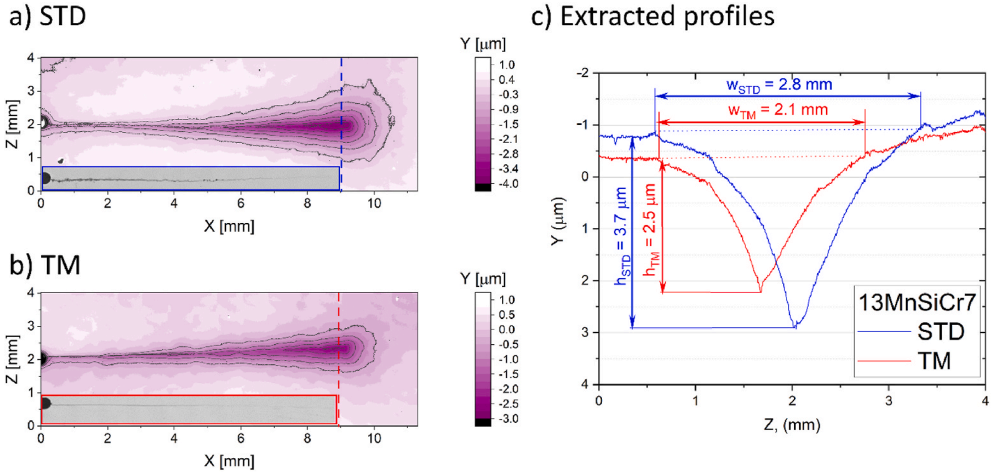

Fig. 6. Topographical mapping of the surface along the fatigue crack of CT-samples of a) STD and b) TM steels. The macroscopic images of the fatigue cracks for both steels are given in the bottom left corners of the topographical mappings (note the jagged fatigue crack in STD steel and fairly straight in TM). Extracted profiles c) of associated lines indicated on the topographical mappings.

referring to the results of EBSD phase maps (Fig. 4). Moreover, it is well known that cleavage fracture occurs in ferrite on {100} planes [34,35]. As a result, when the fatigue crack reaches the ferrite grain with a preferable orientation, it propagates significantly faster due to the brittle fracture. It can also be noticed that occasionally the fatigue crack propagated along the grain boundaries, resulting in intergranular fracture (see Fig. 12d, green ellipses), which can be caused by insufficient cohesion between grains. These regions with intergranular fracture also accelerated the fatigue crack propagation. Thus, the combination of these factors probably contributed to inferior fatigue behavior of STD material in comparison with TM.

The fracture surface of CT-TM-1 sample (Fig. 13) is considerably smoother and more homogeneous in comparison with CT-STD-1 sample. This is consistent with the fact that the fatigue crack in TM material is considerably more linear than in STD (see Fig. 6). No features with cleavage or intergranular type fracture were observed. It must be pointed out that the overall prior austenite grain boundary surface is increased by a factor of 25, if the grain size is reduced to 1/5. Consequently, the average grain boundary concentration of harmful segregated atoms (e.g. phosphorus) lowering grain boundary cohesion (compared to STD steel) than is reduced to 1/25 (4%). This explains why grain boundary decohesion is more likely to occur if the prior austenite grain size is larger. Similar to STD steel, striation lines were detected as well (Fig. 13). However, they are significantly less pronounced. From these lines a crack propagation rates of 70–80 nm/cycle was estimated, which again, matches with values reported in Fig. 5.

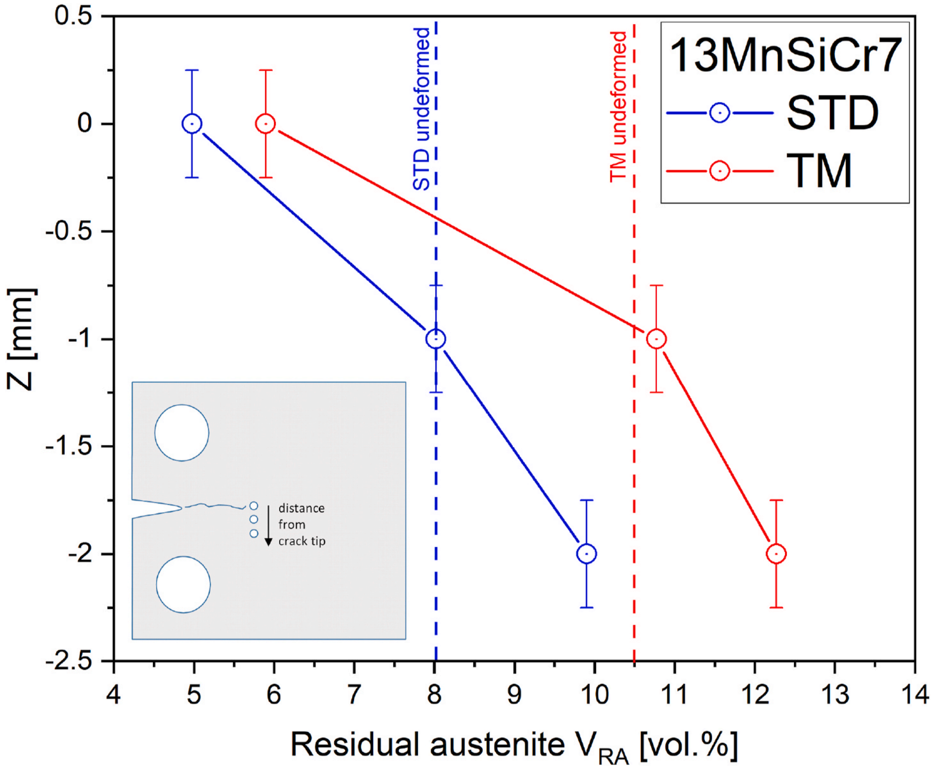

Fig. 7. Determination of the residual austenite at the crack tip of the samples CT-STD-2 and CT-TM-2 using VSM. The average residual austenite content for the undeformed materials is shown with vertical dashed lines. The scale bars correspond to the diameter of cylindrical specimens for VSM (0.5 mm).

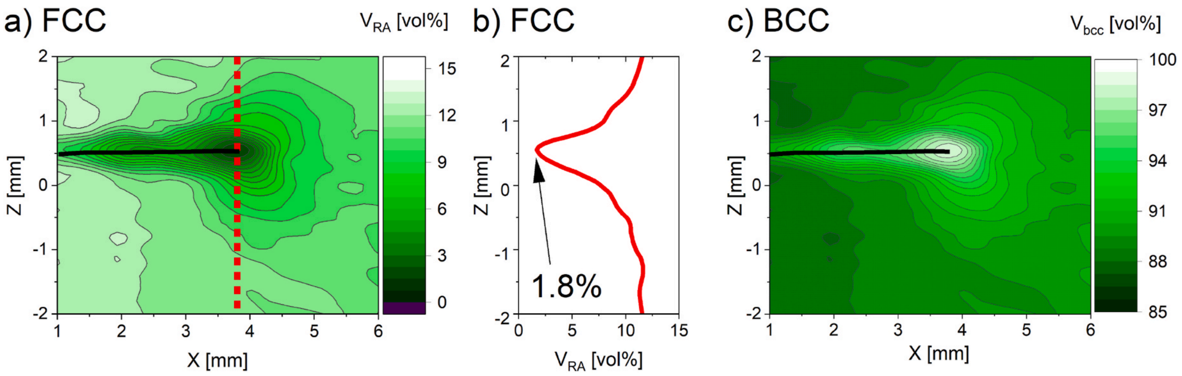

Fig. 8. a) fcc phase fraction in TM steel in the vicinity of the crack tip, b) average fcc content integrated in the marked area, c) bcc phase fraction in TM steel.

4. Discussion

4.1. Influence of grain size on TRIP effect and fatigue crack growth behavior

The results of the fatigue crack growth tests (Fig. 5) indicate an enhanced performance of TM in comparison with STD material. However, it is well known that despite significant improvement in endurance strength, grain refinement can deteriorate the resistance to fatigue crack propagation. Previous studies have proven this for metallic materials with both fcc (e.g. aluminum alloys [36,37] or copper [38]), as well as with bcc (e.g. IF steel [39], or low carbon steel [40]) microstructures. This deterioration is mostly attributed to the small grain size, which hinders the mobility of dislocations and their ability to cross grain boundaries [41]. Thus, the observed improvement in fatigue crack resistance in this work cannot be explained by grain refinement and might be attributed to the TRIP effect.

Plastic deformation of steels with residual austenite can cause its transformation into martensite [42]. Numerous investigations have shown that the TRIP effect can be used to improve the fatigue properties of bainitic TRIP steels [2–4,43]. A significant enhancement of endurance strength, especially upon overloads, was reported in Refs. [44–49]. The associated increase in performance was explained by closure of the fatigue crack tip by compressive stresses due to the phase transformation. The stability of the residual austenite is primarily determined by its chemical composition (particularly carbon content) and grain size [50]. Thus, the finer grains of residual austenite in TM steel are inherently more stable than coarser grains in STD. On the other hand, when the residual austenite grains become too stable, they might not exhibit martensitic transformation [51]. Hence, three main questions arose at the beginning of this investigation: (a) whether the martensitic transformation in TM steel takes place, (b) in how far the TRIP effect contributes to improvement in crack propagation resistance, and (c) how the increased stability of refined residual austenite influences the crack

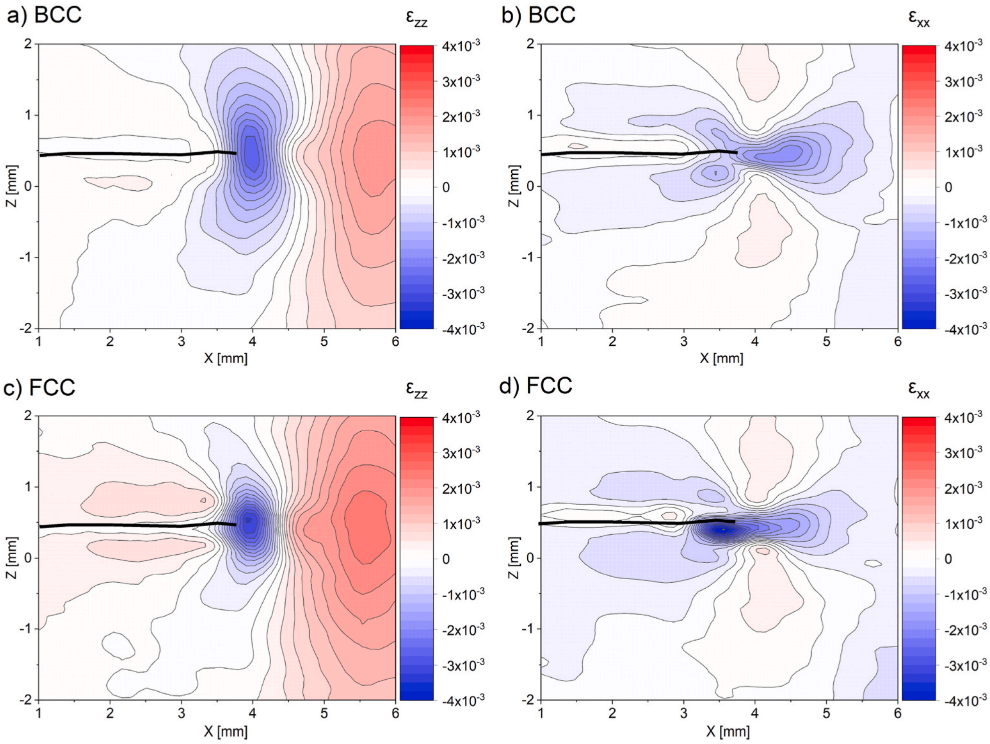

Fig. 9. Strain in bcc phase across the mapped area for the TM steel for the directions a) perpendicular to the crack propagation ε_{zz} and b) parallel to the crack propagation ε_{xx}. The corresponding strain fields in the fcc phase are shown in c) and d), respectively.

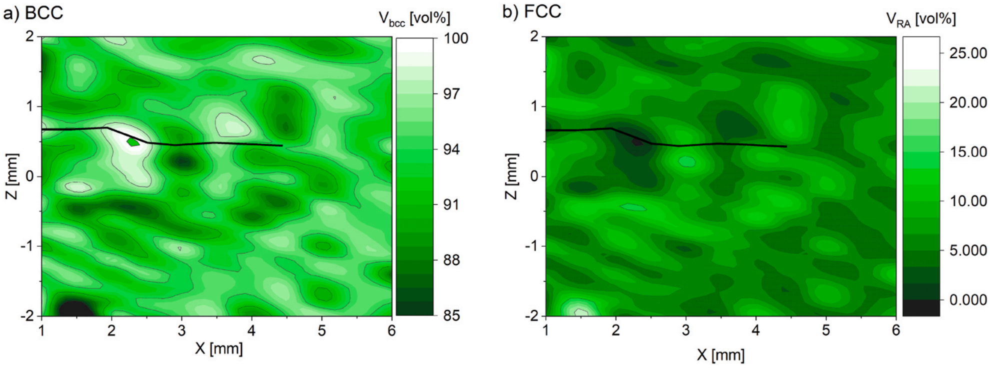

Fig. 10. a) fcc and b) fcc phase fraction in STD steel in the vicinity of the crack tip.

propagation.

In the analytical approach for the calculation of a radius of a plastic zone [52] it is assumed that this radius is a function of the stress intensity factor, yield strength of the material, as well as the stress state (i.e. plane stress/strain). Considering that these parameters are identical or comparable in the CT-STD-1 and CT-TM-1 samples, it is expected that the radii of the plastic zones should be also similar. However, as mentioned above (see Fig. 6), the plastic deformation near the crack tip in STD steel is more pronounced than in TM. The observed discrepancy can be associated with the considerable grain refinement in TM steel. The amount of grains per unit volume of the material increases as the grain size decreases. Thus, the plastic zone near the crack tip in the TM sample interacts with a larger number of grains, and the crack has to pass through more grain boundaries. Furthermore, the microstructure in the TM samples is significantly more homogeneous, which leads to a more uniform distribution of residual stresses near the crack tip.

In order to investigate the microstructure and phase changes in the STD and TM steels, it is important to select appropriate characterization methods. In other studies on TRIP steels, mainly EBSD measurements were used for this purpose [3,43,53]. However, it is obvious from Fig. 4 that it is hardly possible to resolve the residual austenite in both STD and TM steels by EBSD in the present work. Carbon is the main austenite stabilizing element in the investigated steels. Its concentration in the fcc phase is significantly higher (see Table 6) than in the rest of the microstructure, which causes considerable distortion of the austenite lattice. Somewhat higher carbon content of residual austenite in STD steel might indicate its higher stability. The morphology of residual austenite, as well as grain orientation, also play significant role in its stability. The lamellar austenite tend to be more stable than block form [54]. However, due to the limitations of EBSD measurements, no clear conclusions about the morphology of residual austenite in the investigated materials can be made. It is speculated that this strain related distortion of the fcc austenitic phase results in a distortion of the backscattered diffraction patterns, hence, the simulated Kikuchi bands mismatch, or have a low confidence index, and are therefore unidentified and are colored in black in the EBSD map. The elastic strain can be confirmed by the KAM maps. Additionally, EBSD allows only the investigation of the surface layer of the material.

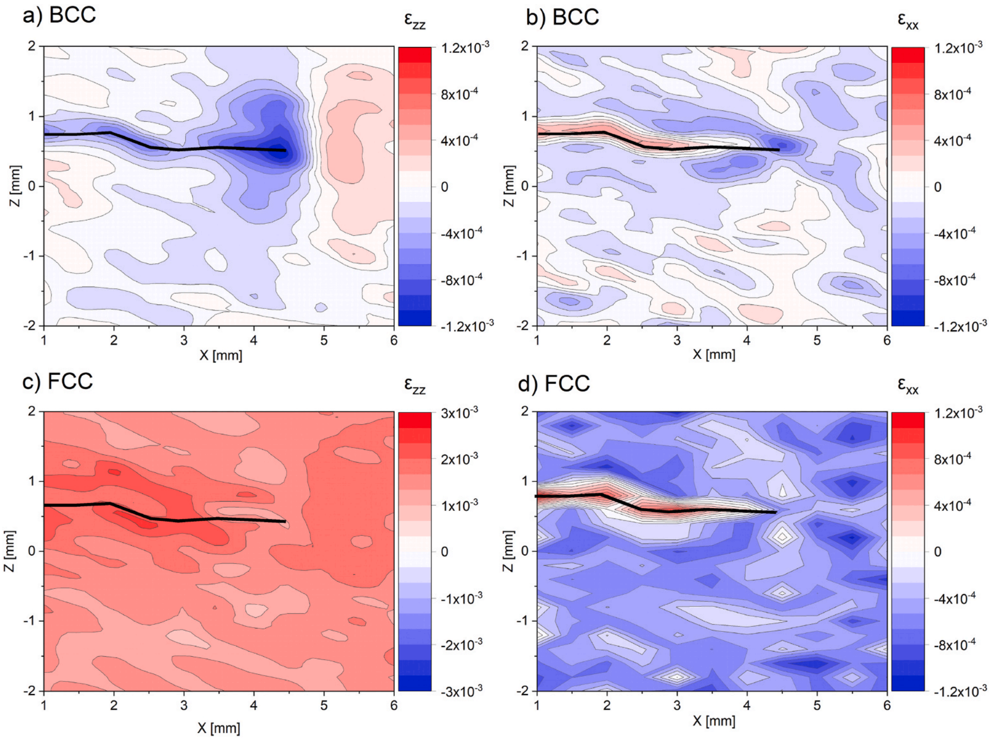

Fig. 11. Strain in bcc phase across the mapped area for the STD steel for the directions a) perpendicular to the crack propagation ε_{zz} and b) parallel to the crack propagation ε_{xx}. The corresponding strain fields in the fcc phase are shown in c) and d), respectively.

Table 5
Estimated residual stresses along respective axes in fcc and bcc phases in STD and TM steels, as well as hydrostatic stress.

Residual stress [MPa]	STD		TM	
	fcc	bcc	fcc	bcc
σ_{xx}	316	−272	−811	−694
σ_{zz}	39	−351	−1005	−885
σ_{yy}	99	−174	−509	−442
σ_{hyd}	151	−266	−775	−674

Table 6
Austenite lattice parameter and austenite carbon content for STD and TM steels.

Steel	a [nm]	C [wt%]
STD	0.36088 ± 0.00010	1.22 ± 0.02
TM	0.36048 ± 0.00007	1.14 ± 0.04

The amount of residual austenite in the investigated steels could be successfully estimated by VSM. For both the STD and TM samples a significant decrease of the amount of austenite by approx. 5 vol% in comparison with the undeformed state clearly indicate the phase transformation near the fatigue crack tip. However, the results of the VSM measurements are rather qualitative than quantitative, due to the rather large sample size for VSM and the limitations with respect to the precision of sample extraction.

HEXRD allowed obtaining high-resolution phase and lattice strain maps of both STD and TM steel. This provided the possibility to quantitatively characterize the effect of the propagating fatigue crack on the phase transformation. For the TM steel, a minimum amount of less than 2 vol% of residual austenite was measured directly at the crack tip, which corroborates the results from the VSM measurements. The austenite-to-martensite phase transformation is more difficult to observe in the STD sample, presumably due to the significantly coarser microstructure. Pronounced compressive strains were measured in the vicinity of the crack tip for both the STD and TM samples. As the result, the material near the crack tip is in the residual three-dimensional stress state (Table 5). Naturally, a significant part of this stress field is caused by extensive plastic deformation as the fatigue crack propagated through the material. However, the volume expansion due to martensitic transformation is also a contributing factor. It is well known that in the multiaxial stress field [55] the stability of the residual austenite decreases, although the local grain orientation plays a significant role. At the same time, higher hydrostatic stress from surrounding microstructure tend to counteract the martensitic transformation [56]. A significant decrease of residual austenite was measured in both STD and TM steels, despite of considerably larger hydrostatic stress component in the latter. This indicates that the stabilization of residual austenite due to large hydrostatic compressive stresses is insufficient to suppress the martensitic transformation in TM steels. The high stress concentration near a crack tip can trigger the transformation process, hence small regions of fcc can transform into bcc. This transformation, and the associated dilatation can cause the crack to close, and thus the overall stress concentration near the crack tip decreases enhancing the fracture toughness, which increases the resistance to fatigue crack growth.

4.2. Contribution of martensitic transformation to fracture toughness

Chen et al. proposed an approach for estimating the effect of the martensitic transformation on fracture toughness of TRIP steel [3]. For this purpose, the following equation was used

$$(\Delta K_c)_{A\rightarrow M} = \sqrt{\Delta R_{A\rightarrow M}\cdot E} = \sqrt{\left(\sigma_m\cdot\frac{\varepsilon_{IS}}{\sqrt{3}}\right)\cdot 2r_p\cdot\overline{V}_M\cdot E} \tag{7}$$

where σ_m is the stress required to initiate the phase transformation (it was assumed to be equal to the yield stress of the corresponding steel in this calculation and given in Table 2), ε_{IS} is the invariant strain associated with the transformation ($\varepsilon_{IS} = 0.2$), r_p is the radius of the monotonic plastic zone, $\overline{V}_M$ the average volume faction of martensite, that was

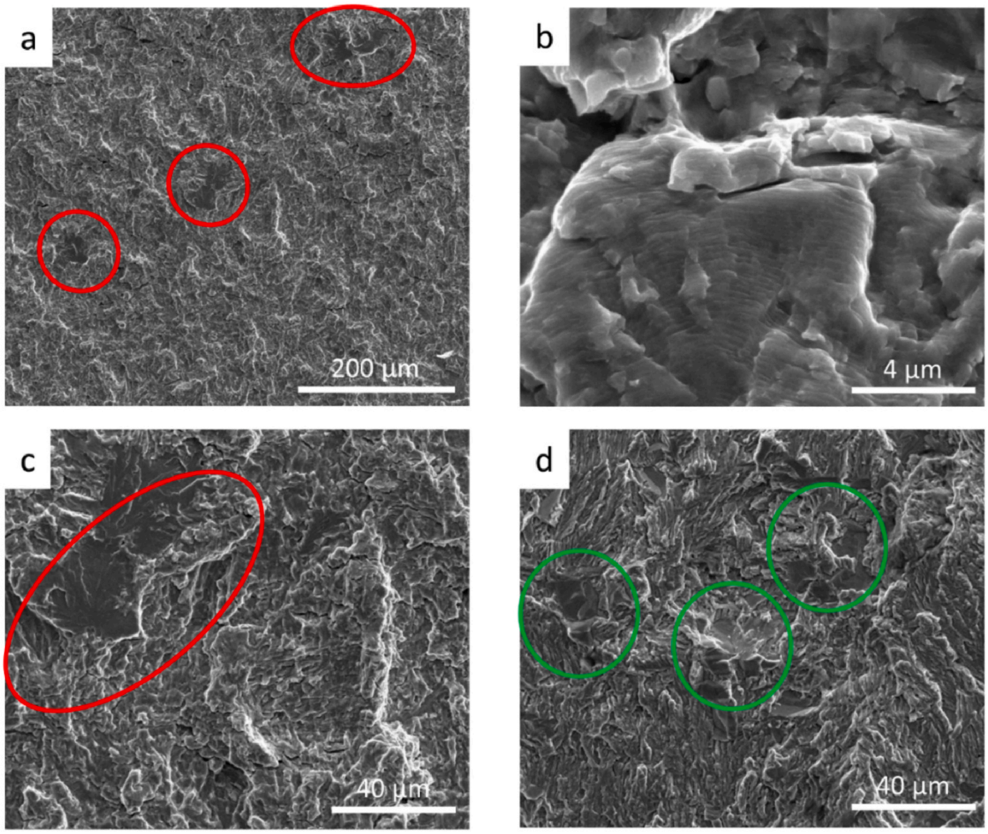

Fig. 12. Fracture surface of sample CT-STD-1. Red ellipses indicate brittle cleavage fracture, while green ellipses indicate intergranular fracture. Crack propagation direction is bottom-top. (For interpretation of the references to color in this figure legend, the reader is referred to the Web version of this article.)

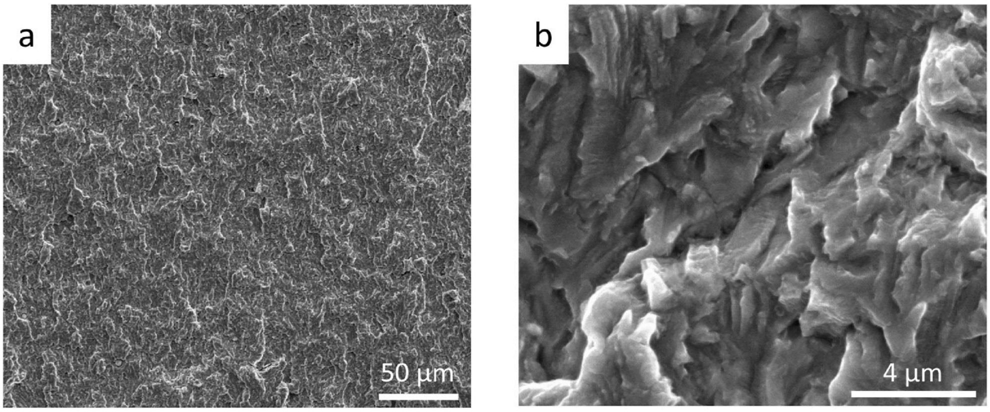

Fig. 13. Fracture surface of sample CT-TM-1. Crack propagation direction is bottom-top.

formed inside the monotonic plastic zone during fracture process, and E is the modulus of elasticity. For the calculations according to this equation, firstly we need to determine two parameters, namely r_p and $\overline{V}_M$.

The profiles of the volume fractions of residual austenite in STD and TM steels are shown in Fig. 14 and were extracted from the HEXRD data presented in Figs. 8 and 10, respectively. Due to pronounced plastic deformation in the plastic zone, the martensitic transformation takes place. Consequently, a decreased austenite content locates near the crack tip. As the distance from the crack tip increases, the content of residual austenite increases too, and reaches the average values of the undeformed STD and TM samples at roughly 1.1 mm and 1.9 mm, respectively. These values correspond reasonably well to the radius of the monotonic plastic zone for plane strain conditions, which can be approximately estimated according to the equation

$$r_p = \frac{1}{3\pi}\left(\frac{K_{max}}{\sigma_y}\right)^2 \tag{8}$$

For the quantitative determination of the amount of RA, the curve fitting of the data was performed using the following function

$$V_{RA} = a - b \cdot c^{\rho} \tag{9}$$

The estimated functions are given in Fig. 14.

The average volume fraction of martensite $\overline{V}_M$ was determined as the difference between the content of residual austenite in the undeformed material and the average amount of the residual austenite in the

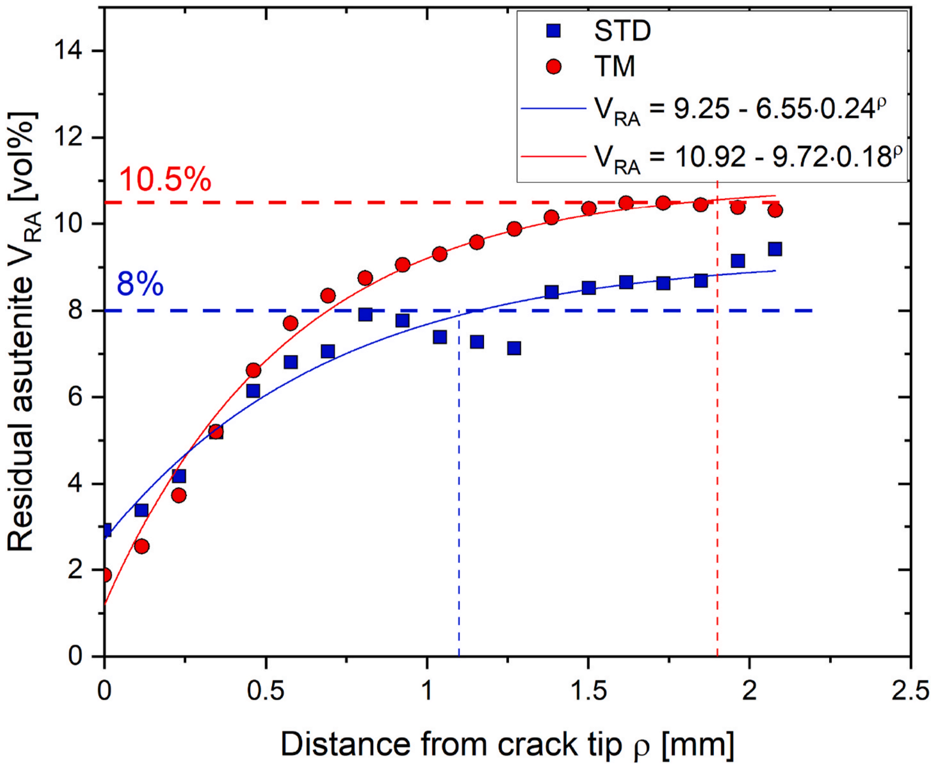

Fig. 14. Volume content of residual austenite as a function of the distance from the crack tip. Thick dash lines indicate average content of residual austenite in steels.

monotonic plastic zone. This resulted in values for $\overline{V}_M$ of 1.9 and 2.9 vol % in the STD and TM samples, respectively.

The fracture toughness of STD and TM samples were experimentally estimated to be 74.4 MPa $m^{0.5}$ and 82.3 MPa $m^{0.5}$, respectively, (see Fig. 5). After performing the calculations according to equation (7), the contribution of phase transformation to the fracture toughness was estimated to be 31.9 MPa $m^{0.5}$ and 43.8 MPa $m^{0.5}$, i.e. 42% and 53%, correspondingly. Thus, it can be concluded that the TRIP effect in TM steel contributes significantly more to the improved fatigue crack resistance. Taking into account the residual austenite contents in the bulk material (8 vol% vs. 10.5 vol%), the increases in fracture toughness are 4.0 MPa $m^{0.5}$ (STD) and 4.2 MPa $m^{0.5}$ (TM) per vol% of residual austenite. At the same time, the TM steel has larger amount of residual austenite, as well as higher volume fraction of transformed martensite, compared to STD steel. Subsequently, we can assess the specific increase of fracture toughness per vol% of transformation induced martensite, which results to 16.8 MPa $m^{0.5}$ per vol% for STD and 15.1 MPa $m^{0.5}$ per vol% for TM. This results indicates that the retained austenite in TM is more stable, although the difference is small.

5. Conclusions

In this study, two low-alloyed bainitic TRIP-assisted steels with identical chemical compositions but with different processing methods have been investigated: the reference (STD) steel was conventionally rolled, whereas new micro-bainitic TRIP steel (TM) underwent additional thermomechanical treatment (was re-rolled) using a novel XTP® technology. Consequently, the investigated steels had significant differences in microstructure (in terms of residual austenite content, as well as grain size), which allowed to estimate the effects of grain refinement on their crack propagation properties. The main results can be summarized as follows:

1. Lowering the hot rolling temperature from 1′100 °C–800 °C by applying the XTP® technology, the retained austenite content of new micro-bainitic TRIP steel could be increased by ~30%.
2. After applying the thermomechanical treatment to the STD steel, the TM steel showed an improvement of the fatigue crack propagation properties (i.e. threshold K_{th}, crack propagation rate, and fracture toughness K_{Ic}).
3. While EBSD proved to have limitations to quantify the amount of the highly distorted residual austenite, the austenite volume fraction and the amount of martensite in the vicinity of the fatigue crack could be successfully estimated by VSM and HEXRD.
4. The estimated total contribution of the TRIP effect to the fracture toughness is higher in TM steel than in STD steel. This can be explained by higher residual austenite content (10.5 vol% for TM and 8 vol% for STD). The fracture toughness rises by 4 MPa $m^{0.5}$ for each 1 vol% increase in residual austenite.
5. By applying the additional thermomechanical treatment the occurrence of cleavage fracture could be reduced. This might be explained with a reduced grain boundary concentration of segregated and embrittleling atoms.

CRediT authorship contribution statement

I. Burda: Conceptualization, Methodology, Data curation, Visualization, Investigation, Formal analysis, Writing – original draftK. Zweiacker: Methodology, Investigation, Data curation, Visualization, Writing – review & editingA. Arabi-Hashemi: Methodology, Investigation, Data curation, Writing – review & editingP. Barriobero Vila: Methodology, Writing – review & editingA. Stutz: Methodology, Investigation, Writing – review & editingR. Koller: Project administration, Funding acquisition, Writing – review & editing H. Roelofs: Resources, Project administration, Writing – review & editingL. Oberli: Methodology, Writing – review & editingM. Lembke: Methodology, Writing – review & editingC. Affolter: Project administration, Writing – review & editingC. Leinenbach: Project administration, Funding acquisition,

Resources, Writing – original draft.

Data availability

The data will be made available upon reasonable request.

Declaration of competing interest

The authors declare that they have no known competing financial interests or personal relationships that could have appeared to influence the work reported in this paper.

Acknowledgement

The work was supported by the Swiss Innovation Agency (project number 27126.1 PFIW-IW), which is gratefully acknowledged.

Appendix A. Supplementary data

Supplementary data to this article can be found online at https://doi.org/10.1016/j.msea.2022.142898.

References

[1] E. Girault, A. Mertens, P. Jacques, Y. Houbaert, B. Verlinden, J. Van Humbeeck, Comparison of the effects of silicon and aluminium on the tensile behaviour of multiphase TRIP-assisted steels, Scripta Mater. 44 (2001) 885–892, https://doi.org/10.1016/S1359-6462(00)00697-7.

[2] B. Yan, D. Urban, Characterization OF fatigue and crash performance OF new generation high strength steels for automotive applications, AISIDOE Technol. Roadmap Program Rep. (2003) 97.

[3] X. Cheng, R. Petrov, L. Zhao, M. Janssen, Fatigue crack growth in TRIP steel under positive R-ratios, Eng. Fract. Mech. 75 (2008) 739–749, https://doi.org/10.1016/j.engfracmech.2007.01.019.

[4] K. Sugimoto, D. Fiji, N. Yoshikawa, Fatigue strength of newly developed high-strength low alloy TRIP-aided steels with good hardenability, Procedia Eng. 2 (2010) 359–362, https://doi.org/10.1016/j.proeng.2010.03.040.

[5] T. Iwamoto, T. Tsuta, Computational simulation of the dependence of the austenitic grain size on the deformation behavior of TRIP steels, Int. J. Plast. 16 (2000) 791–804, https://doi.org/10.1016/S0749-6419(99)00079-0.

[6] H. Mughrabi, H.W. Höppel, Cyclic deformation and fatigue properties of ultrafine grain size materials: current status and some criteria for improvement of the fatigue resistance, MRS Online Proc. Libr. OPL 634 (2000), https://doi.org/10.1557/PROC-634-B2.1.1.

[7] T. Niendorf, Ermüdungseigenschaften ultrafeinkörniger kubisch raumzentrierter Werkstoffe : Einfluss der Mikrostruktur, 2010. http://digital.ub.uni-paderborn.de/hsmig/1764. (Accessed 5 May 2021). accessed.

[8] T. Niendorf, H.J. Maier, D. Canadinc, I. Karaman, On the cyclic stability and fatigue performance of ultrafine-grained interstitial-free steel under mean stress, 378–379, Key Eng. Mater. (2008) 39–52, https://doi.org/10.4028/www.scientific.net/KEM.378-379.39.

[9] T. Niendorf, D. Canadinc, H.J. Maier, I. Karaman, S.G. Sutter, On the fatigue behavior of ultrafine-grained interstitial-free steel, Int. J. Mater. Res. 97 (2006) 1328–1336, https://doi.org/10.3139/146.101377.

[10] T. Sawai, S. Matsuoka, K. Tsuzaki, Low-and high-cycle fatigue properties of ultrafine-grained low carbon steels, Tetsu–HaganeJournal Iron Steel Inst, Jpn. 89 (2003) 726–733, https://doi.org/10.2355/tetsutohagane1955.89.6_726.

[11] M.D. Chapetti, H. Miyata, T. Tagawa, T. Miyata, M. Fujioka, Fatigue strength of ultra-fine grained steels, Mater. Sci. Eng. 381 (2004) 331–336, https://doi.org/10.1016/j.msea.2004.04.055.

[12] D. Geist, C. Rentenberger, H.P. Karnthaler, Extreme structural inhomogeneities in high-pressure torsion samples along the axial direction, Acta Mater. 59 (2011) 4578–4586, https://doi.org/10.1016/j.actamat.2011.04.003.

[13] Y. Cao, M. Kawasaki, Y.B. Wang, S.N. Alhajeri, X.Z. Liao, W.L. Zheng, S.P. Ringer, Y.T. Zhu, T.G. Langdon, Unusual macroscopic shearing patterns observed in metals processed by high-pressure torsion, J. Mater. Sci. 45 (2010) 4545–4553, https://doi.org/10.1007/s10853-010-4485-5.

[14] P.R. Cetlin, M.T.P. Aguilar, R.B. Figueiredo, T.G. Langdon, Avoiding cracks and inhomogeneities in billets processed by ECAP, J. Mater. Sci. 45 (2010) 4561–4570, https://doi.org/10.1007/s10853-010-4384-9.

[15] Y. Cao, Y.B. Wang, S.N. Alhajeri, X.Z. Liao, W.L. Zheng, S.P. Ringer, T.G. Langdon, Y.T. Zhu, A visualization of shear strain in processing by high-pressure torsion, J. Mater. Sci. 45 (2010) 765–770, https://doi.org/10.1007/s10853-009-3998-2.

[16] S. Torizuka, M. Kuntz, Y. Furuya, M. Bacher-Hoechst, Effect of tensile strength and microstructure on notch-fatigue properties of ultrafine-grained steels, ISIJ Int. 52 (2012) 910–914, https://doi.org/10.2355/isijinternational.52.910.

[17] Y. Furuya, S. Matsuoka, S. Shimakura, T. Hanamura, S. Torizuka, Fatigue strength of ultrafine ferrite-cementite steels and effects of strengthening mechanisms, Metall. Mater. Trans. 38 (2007) 2984–2991, https://doi.org/10.1007/s11661-007-9355-7.

[18] Y. Furuya, S. Matsuoka, S. Shimakura, T. Hanamura, S. Torizuka, Effects of carbon and phosphorus addition on the fatigue properties of ultrafine-grained steels, Scripta Mater. 52 (2005) 1163–1167, https://doi.org/10.1016/j.scriptamat.2005.01.035.

[19] C. Ruffing, Schwingfestigkeit und Mikrostruktur von ultrafeinkörnigem C45, 2015. https://kluedo.ub.uni-kl.de/frontdoor/index/index/year/2015/docId/4038. (Accessed 5 May 2021). accessed.

[20] R. Rozmus, R. Kuziak, L. Oberli, H. Roelofs, New Fine Grained Temper-Resistant Long Products, Darmstadt, 2018.

[21] A. Borowikow, H. Blei, Integration of screw rolling in the thermo-mechanical treatment of steel bars, Roll Pass Des. 72 (2011) 53–60.

[22] S.P. Galkin, B.A. Romantsev, A. Borowikow, New Inline Process for Thermomechanical Treatment of Steel Bars, vol. 1, CIS Iron Steel Rev, 2012. http://www.rudmet.ru/journal/996/article/15687/. (Accessed 5 May 2021). accessed.

[23] M. Lembke, L. Oberli, G. Olschewski, Probing the limits of steel by producing an ultrafine microstructure in a single extreme deformation step, in: Future Trends Steel Dev. Process. Technol. Appl. Bringing Automot. Supplier Steel Ind. Together 5th SCT 2017 5th Int. Conf. Steels Cars Trucks Proc, 2017.

[24] M. Lembke, Ultrafeinkörnige thermomechanisch behandelte Langprodukte mit hohen Zähigkeitswerten, in: Werkst, 2017. Dresden, 2017.

[25] ISO, DIN EN ISO 6892-1:2020 - Metallische Werkstoffe – Zugversuch –, Deutsches Institut für Normung, n.d. https://doi.org/10.1520/E0647-15E01.

[26] DIN, DIN 50125 - Prüfung Metallischer Werkstoffe – Zugproben, Deutsches Institut für Normung, n.d. https://doi.org/10.1520/E0647-15E01.

[27] ASTM, ASTM 647-15 Test Method for Measurement of Fatigue Crack Growth Rates, ASTM International, n.d. https://doi.org/10.1520/E0647-15E01.

[28] E.M. Lehockey, Y.-P. Lin, O.E. Lepik, Mapping residual plastic strain in materials using electron backscatter diffraction, in: A.J. Schwartz, M. Kumar, B.L. Adams (Eds.), Electron Backscatter Diffr. Mater. Sci., Springer US, Boston, MA, 2000, pp. 247–264, https://doi.org/10.1007/978-1-4757-3205-4_20.

[29] S. Foner, Versatile and sensitive vibrating-sample magnetometer, Rev. Sci. Instrum. 30 (1959) 548–557, https://doi.org/10.1063/1.1716679.

[30] L. Zhao, N.H. van Dijk, E. Brück, J. Sietsma, S. van der Zwaag, Magnetic and X-ray diffraction measurements for the determination of retained austenite in TRIP steels, Mater. Sci. Eng. 313 (2001) 145–152, https://doi.org/10.1016/S0921-5093(01)00965-0.

[31] J. Gussone, K. Bugelnig, P. Barriobero-Vila, J.C. da Silva, U. Hecht, C. Dresbach, F. Sket, P. Cloetens, A. Stark, N. Schell, J. Haubrich, G. Requena, Ultrafine eutectic Ti-Fe-based alloys processed by additive manufacturing – a new candidate for high temperature applications, Appl. Mater. Today 20 (2020) 100767, https://doi.org/10.1016/j.apmt.2020.100767.

[32] R. Petrov, L. Kestens, A. Wasilkowska, Y. Houbaert, Microstructure and texture of a lightly deformed TRIP-assisted steel characterized by means of the EBSD technique, Mater. Sci. Eng. 447 (2007) 285–297, https://doi.org/10.1016/j.msea.2006.10.023.

[33] D.B. Cullity, S.R. Stock, Elements of X-Ray Diffraction. third ed. |, Pearson, n.d. https://www.pearson.com/uk/educators/higher-education-educators/program/Cullity-Elements-of-X-Ray-Diffraction-International-Edition-3rd-Edition/PGM615091.html (accessed February 9, 2022).

[34] C.O.A. Semprimoschnig, J. Stampfl, R. Pippan, O. Kolednik, A new powerful tool for surveying cleavage fracture surfaces, Fatig. Fract. Eng. Mater. Struct. 20 (1997) 1541–1550, https://doi.org/10.1111/j.1460-2695.1997.tb01509.x.

[35] Y.J. Park, I.M. Bernstein, The process of crack initiation and effective grain size for cleavage fracture in pearlitic eutectoid steel, Metall. Trans. A 10 (1979) 1653–1664, https://doi.org/10.1007/BF02811698.

[36] Y. Estrin, A. Vinogradov, Fatigue behaviour of light alloys with ultrafine grain structure produced by severe plastic deformation: an overview, Int. J. Fatig. 32 (2010) 898–907, https://doi.org/10.1016/j.ijfatigue.2009.06.022.

[37] K. Hockauf, M.F.-X. Wagner, T. Halle, T. Niendorf, M. Hockauf, T. Lampke, Influence of precipitates on low-cycle fatigue and crack growth behavior in an ultrafine-grained aluminum alloy, Acta Mater. 80 (2014) 250–263, https://doi.org/10.1016/j.actamat.2014.07.061.

[38] M. Arzaghi, C. Sarrazin-Baudoux, J. Petit, Fatigue crack growth in ultrafine-grained copper obtained by ECAP, Adv. Mater. Res. 891–892 (2014) 1099–1104. https://doi.org/10.4028/www.scientific.net/AMR.891-892.1099.

[39] T. Niendorf, F. Rubitschek, H.J. Maier, D. Canadinc, I. Karaman, On the fatigue crack growth–microstructure relationship in ultrafine-grained interstitial-free steel, J. Mater. Sci. 45 (2010) 4813–4821, https://doi.org/10.1007/s10853-010-4511-7.

[40] H.-K. Kim, M.-I. Choi, C.-S. Chung, D.H. Shin, Fatigue properties of ultrafine grained low carbon steel produced by equal channel angular pressing, Mater. Sci. Eng. 340 (2003) 243–250, https://doi.org/10.1016/S0921-5093(02)00178-8.

[41] T. Niendorf, D. Canadinc, H.J. Maier, Fatigue damage evolution in ultrafine-grained interstitial-free steel, Adv. Eng. Mater. 13 (2011) 275–280, https://doi.org/10.1002/adem.201000272.

[42] F.D. Fischer, Q.-P. Sun, K. Tanaka, Transformation-induced plasticity (TRIP), Appl. Mech. Rev. 49 (1996) 317–364, https://doi.org/10.1115/1.3101930.

[43] T.B. Hilditch, I.B. Timokhina, L.T. Robertson, E.V. Pereloma, P.D. Hodgson, Cyclic deformation of advanced high-strength steels: mechanical behavior and microstructural analysis, Metall. Mater. Trans. 40 (2009) 342–353, https://doi.org/10.1007/s11661-008-9732-x.

[44] V. Wirths, Prozessführung und zyklisches Werkstoffverhalten von karbidfreien bainitischen Stählen, Dissertation, Rheinisch-Westfälische Technische Hochschule

Aachen, 2016–2017. https://publications.rwth-aachen.de/record/678237. (Accessed 5 May 2021). accessed.

[45] V. Wirths, W. Bleck, R. Wagener, T. Melz, Bainitic forging steels, Aachen, in: 29 Aachen. Stahlkolloquium Steel Compet., 2014.

[46] V. Wirths, W. Bleck, R. Wagener, T. Melz, Carbide Free Bainitic Forging Steels with Improved Fatigue Properties, Steels Cars Trucks, 2014, 2015.

[47] V. Wirths, W. Bleck, R. Wagener, T. Melz, Forging Steels with Carbide Free Bainite for High Service Fatigue Life Properties, 1st ESTAD 31st JSI, 2014.

[48] V. Wirths, L. Elek, Schmiedestähle mit verbesserter Betriebsfestigkeit durch verformungsinduzierte Phasenumwandlung, Forschungsgesellschaft Stahlverformung e.V, Hagen, 2014.

[49] V. Wirths, R. Wagener, W. Bleck, T. Melz, Bainitic forging steels for cyclic loading, Adv. Mater. Res. 922 (2014) 813–818. https://doi.org/10.4028/www.scientific.net/AMR.922.813.

[50] J. Wang, P.J. Van Der Wolk, S. Van Der Zwaag, On the influence of alloying elements on the bainite reaction in low alloy steels during continuous cooling, J. Mater. Sci. 35 (2000) 4393–4404, https://doi.org/10.1023/A:1004865209116.

[51] J. Wang, S. Van Der Zwaag, Stabilization mechanisms of retained austenite in transformation-induced plasticity steel, Metall. Mater. Trans. 32 (2001) 1527–1539, https://doi.org/10.1007/s11661-001-0240-5.

[52] D. Broek, The Practical Use of Fracture Mechanics, Springer Netherlands, 1988.

[53] G.K. Tirumalasetty, M.A. van Huis, C. Kwakernaak, J. Sietsma, W.G. Sloof, H. W. Zandbergen, Deformation-induced austenite grain rotation and transformation in TRIP-assisted steel, Acta Mater. 60 (2012) 1311–1321, https://doi.org/10.1016/j.actamat.2011.11.026.

[54] Z.J. Xie, Y.Q. Ren, W.H. Zhou, J.R. Yang, C.J. Shang, R.D.K. Misra, Stability of retained austenite in multi-phase microstructure during austempering and its effect on the ductility of a low carbon steel, Mater. Sci. Eng. 603 (2014) 69–75, https://doi.org/10.1016/j.msea.2014.02.059.

[55] P.J. Jacques, Q. Furnémont, F. Lani, T. Pardoen, F. Delannay, Multiscale mechanics of TRIP-assisted multiphase steels: I. Characterization and mechanical testing, Acta Mater. 55 (2007) 3681–3693, https://doi.org/10.1016/j.actamat.2007.02.029.

[56] X.C. Xiong, B. Chen, M.X. Huang, J.F. Wang, L. Wang, The effect of morphology on the stability of retained austenite in a quenched and partitioned steel, Scripta Mater. 68 (2013) 321–324, https://doi.org/10.1016/j.scriptamat.2012.11.003.